





Article

# Microstructure and Mechanical Properties of Sintered and Heat-Treated HfNbTaTiZr High Entropy Alloy

Jaroslav Málek <sup>1,2,\*</sup> , Jiří Zýka <sup>1</sup> , František Lukáč <sup>3,4</sup> , Jakub Čížek <sup>4</sup> , Lenka Kunčická <sup>5</sup> and Radim Kocich <sup>6</sup>

<sup>1</sup> UJP PRAHA a.s., Nad Kamínkou 1345, 156 10 Prague-Zbraslav, Czech Republic; zyka@ujp.cz

<sup>2</sup> CTU in Prague-Faculty of Mechanical Engineering, Karlovo náměstí 13, 121 35 Praha 2, Czech Republic

<sup>3</sup> Institute of Plasma Physics CAS, Za Slovankou 3, 182 00 Praha 8, Czech Republic; lukac@ipp.cas.cz

<sup>4</sup> Faculty of Mathematics and Physics, Charles University, V Holešovičkách 2, 180 00 Praha 8, Czech Republic; jakub.cizek@mff.cuni.cz

<sup>5</sup> Institute of Physics of Materials, CAS, Žitkova 22, 616 00 Brno, Czech Republic; kuncicka@ipm.cz

<sup>6</sup> VŠB-Technical University of Ostrava, 17. Listopadu 15, 708 33 Ostrava 8, Czech Republic; radim.kocich@vsb.cz

\* Correspondence: jardamalek@seznam.cz; Tel.: +420-7778-20414

Received: 25 October 2019; Accepted: 5 December 2019; Published: 7 December 2019



**Abstract:** High entropy alloys (HEAs) have attracted researchers' interest in recent years. The aim of this work was to prepare the HfNbTaTiZr high entropy alloy via the powder metallurgy process and characterize its properties. The powder metallurgy process is a prospective solution for the synthesis of various alloys and has several advantages over arc melting (e.g., no dendritic structure, near net-shape, etc.). Cold isostatic pressing of blended elemental powders and subsequent sintering at 1400 °C for various time periods up to 64 h was used. Certain residual porosity, as well as bcc2 (Nb- and Ta-rich) and hcp (Zr- and Hf-rich) phases, remained in the bcc microstructure after sintering. The bcc2 phase was completely eliminated during annealing (1200 °C/1h) and subsequent water quenching. The hardness values of the sintered specimens ranged from 300 to 400 HV10. The grain coarsening during sintering was significantly limited and the maximum average grain diameter after 64 h of sintering was approximately 60 µm. The compression strength at 800 °C was 370 MPa and decreased to 47 MPa at 1200 °C. Porosity can be removed during the hot deformation process, leading to an increase in hardness to ~450 HV10.

**Keywords:** high entropy alloys; sintering; microstructure

## 1. Introduction

The concept of the so-called “high entropy alloys” (HEAs), also known as “multi-principal element alloys” (MPEAs) or “complex concentrated alloys” (CCAs) [1], has been attracting attention since its formulation in the early 2000s by Yeh et al. [2] and Cantor et al. [3]. The concept of HEAs is different from other alloys of modern structural materials (e.g., composites) which may also consist of multiple metallic elements [4,5]. The traditional design of new alloys with one principal element is replaced by a new group of materials with multiple elements. HEAs typically contain at least five elements with equimolar or near equimolar (5–35 at.%) concentrations [1,6]. Numerous parameters were proposed by various authors in order to predict whether an alloy will exhibit a microstructure consisting of a solid solution with no intermetallic phases [1,7–10]. The matrixes of high entropy alloys are typically bcc or fcc, but recently even HEAs with the hcp matrix have been reported [1,11–14]. The HEAs with the bcc matrix usually exhibit high strength and lower plasticity whereas fcc HEAs have lower strength and high plasticity [1,6].

HEAs exhibit intriguing combinations of properties and structural phenomena; high lattice distortions or sluggish diffusion effects are frequently reported (among others [6]). Such properties are usually attributed to their high entropy and its related effects. As a result of these phenomena, HEAs have the potential to be used in many applications (e.g., high temperature materials, cryogenic materials, etc.) [1,6]. The HfNbTaTiZr equimolar alloy belongs to a bcc structure family of HEAs. It is a promising high entropy alloy with advantageous prospective usage. Given its composition consisting of refractory metals with melting points above 1850 °C [1,15,16], this particular HEA is a promising refractory alloy which can possibly be used to substitute tungsten-based alloys in selected applications [17]. This alloy exhibits quite high tensile strength at room temperature. However, the values reported by various authors are broadly scattered. Dirras et al. [18] reported a tensile strength of 850 MPa, as well as Schuh et al. [19], reaching even 1900 MPa after cold deformation. Those properties were strongly influenced by the microstructure. Senkov et al. [20] showed that the tensile strength of this alloy may reach 1150 MPa by retaining ~15% of elongation after suitable thermo-mechanical processing. Very good combinations of high tensile strength and elongation have also been reported by other authors [21–23]. Excellent compression strength values at elevated temperatures (i.e., 535 MPa at 800 °C or 295 MPa at 1000 °C) were also reported by Senkov et al. [16]. The HfNbTaTiZr alloy contains only biocompatible elements. Its biocompatibility presupposes the alloy also for biomedical applications [24–26]. Therefore, HfNbTaTiZr can be considered as a modern biocompatible material, together with other innovative titanium-based alloys [27,28].

HEAs are usually prepared via arc melting processes, which often results in an inhomogeneous dendritic microstructure [15,18,22,29–40]. The dendritic microstructures are usually removed by subsequent heat treatment. However, in some cases, the dendritic structure is not fully removed after annealing and significant grain coarsening can also be introduced during annealing [16,31,33,38]. It has been reported that large grain size is not desirable for most (not for all) applications as, in most cases, fine grains improve strength and ductility [22,23]. Nevertheless, modern manufacturing methods, such as powder metallurgy technologies [41] and specialized deformation methods (methods of severe plastic deformation—SPD) [42], can be used to refine the structures and enhance the mechanical properties of the processed materials.

Powder metallurgy is a prospective method for the production of metallic materials as it may overcome some of the negative aspects of arc melting (e.g., coarse grains, dendritic structure) [43]. Spark plasma sintering (SPS) and metal injection moulding (MIM) are the most frequently used powder metallurgy technologies, along with others. Only a few works using the powder metallurgy process for the synthesis of HfNbTaTiZr (or similar) HEAs have been reported to date (e.g., [9,43]). Our previous works reported on the preparation of the HfNbTaTiZr equimolar alloy via the arc melting [44–46] and SPS [47] processes. However, the disadvantage of the SPS technology is complicated powder preparation. The powder of the HfNbTaTiZr alloy is currently not commercially available and it is difficult (and expensive) to obtain—usually from gas atomization of the arc melted alloy. Due to these reasons, the present work is focused on the preparation of the HfNbTaTiZr alloy from elemental powders which are commercially available. The aim of this work was to synthesize the HfNbTaTiZr alloy via the blended elemental powder metallurgy process and to evaluate the influence of the process parameters (mainly sintering time) on the microstructure and mechanical properties of the final product.

## 2. Materials and Methods

The samples of the HfNbTaTiZr alloy were prepared via the powder metallurgy process. Elemental powders (granularity: 325 mesh, i.e., grain size <44 µm; purity: min. 99.5%) with irregular shape (HDH powders) were supplied by Huarui Industrial Materials Co., Ltd. (Chengdu, China). The powders were weighted to obtain the desired chemical composition of the equimolar HfNbTaTiZr alloy, mixed in a Turbula 2F device (WAB GmbH, Basel, Switzerland), and filled into the cylinder-shaped molds (inner diameter: 20 mm). These preparation steps were performed under an Ar protective

atmosphere. The specimens were cold isostatically pressed (CIP) using a pressure of 400 MPa and subsequently sintered. The sintering was performed in a vacuum (better than  $10^{-3}$  Pa) furnace at 1400 °C (with 20 °C/min heating rate) for 2, 4, 8, 16, 32 and 64 h (corresponding samples were denoted as “2 h”, “4 h”, “8 h”, “16h”, “32h” and “64h”, respectively). The sintered specimens were further annealed under the argon protective atmosphere at 1200 °C for 1 h and subsequently water quenched. The latter specimens were denoted by the sintering period and a suffix “1200 °C/1h/WQ”.

The microstructure of the specimens was studied by light microscopy (LM) using a Nikon EPIPHOT 3000 microscope (Nikon, Melville, New York, NY, USA) and scanning electron microscopy (SEM) using a JEOL 7650F (JEOL, Akishima, Tokyo, Japan) scanning electron microscope equipped with an electron back scatter diffraction (EBSD) detector Nordlys II (Oxford Instruments, Abingdon on Thames, UK). The SEM observations were done in back-scattered electron mode (BSE) unless otherwise noted. NIS Elements software (Nikon, Melville, New York, NY, USA) was used for image analysis. The specimens for LM and SEM observations were prepared by a standard metallographic process (ground up to #4000 with SiC papers and polished with Struers OP-S emulsion with the addition of H<sub>2</sub>O<sub>2</sub>). For etching, 3 mL of HF + 8 mL of HNO<sub>3</sub> + 100 mL of H<sub>2</sub>O etchants were used. Some specimens were also observed using a JEOL 2000 EX (JEOL, Akishima, Tokyo, Japan) transmission electron microscope (TEM) to provide a more detailed microstructure characterization. The specimens for TEM were ground to a thickness of ~100 µm and appropriate dimensions for the JEOL EM-09100 Ion Slicer (JEOL, Akishima, Tokyo, Japan), where the specimens were thinned to a final thickness. The phase identification was also carried out using X-ray diffraction analysis (XRD) on a Bruker D8 Discover diffractometer (Bruker, Karlsruhe, Germany) using a Cu anode divergent beam aimed at the polished cross section of a bar. Quantitative Rietveld refinement analysis was performed by TOPAS V5 software (Bruker, Karlsruhe, Germany). The Differential Scanning Calorimetry (DSC) method was carried out on Setaram Labsys Evo apparatus (Setaram, Caluire, France) in order to obtain information about the phase stability. The samples were heated in Al<sub>2</sub>O<sub>3</sub> crucibles with a heating rate of 7 °C/min in an Ar flow of 100 mL/min.

The Vickers hardness was determined using a Zwick/Roell ZHU 250 top hardness tester (Zwick/Roell, Ulm, Germany) with a load of 98.1 N (according to the ISO 6507 standard). At least seven values were determined for each measurement. The compression tests were carried out using Zwick furnaces (Zwick/Roell, Ulm, Germany) in the Ar protective atmosphere at the temperatures of 800, 900, 1000, 1100 and 1200 °C and a strain rate of  $10^{-4}$ . The samples for the compression test were 10 mm long and had a circular cross-section with the area of 80 mm<sup>2</sup>. Given the relatively low strain rate, the samples had the tendency to exhibit creep behavior. Due to this, the compression tests were all terminated after 90 min of load exposure.

The oxygen content in the sintered specimens was determined by a Bruker Galileo G8 gas fusion analyzer (Bruker, Karlsruhe, Germany). At least three measurements for each specimen were performed.

The grain size was measured using the line intercept method from at least five images from different regions of the specimen. The images covered a minimum area of 800 µm × 600 µm. The image analysis was used to determine the porosity (the same images as for grain size determination were used).

### 3. Results

The microstructure of the processed specimens is described first, followed by the presentation of the mechanical properties which are supposed to correlate with the microstructure.

#### 3.1. Microstructure

The specimens exhibited certain residual porosity after sintering (determined by the image analysis of at least five light micrographs for each value). The results are shown in Figure 1. The pores had typical dimensions up to 50 µm. Most of the pores were between 10 and 30 µm.

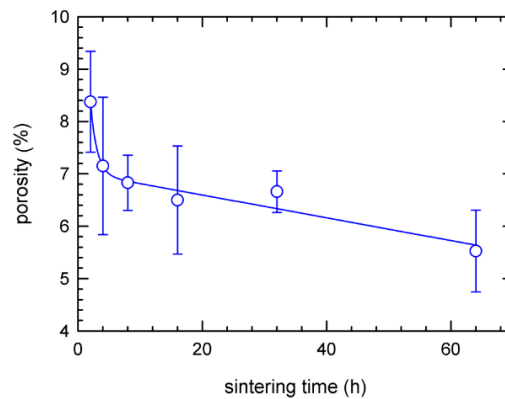


**Figure 1.** The development of porosity vs. sintering time at 1400 °C.

The oxygen content was measured for the sintered and as-pressed (sintering time 0h) specimens. A slightly increasing oxygen content with an increasing sintering time can be seen in Figure 2 (despite the large experimental scatter).

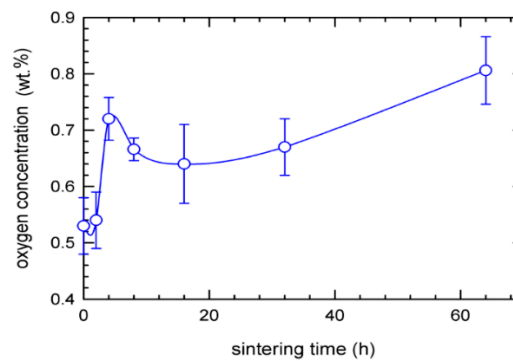


**Figure 2.** Measured oxygen content vs. sintering time in as-sintered specimens.

The microstructure of the as-sintered specimens underwent changes during the sintering process. The original mixture of pressed elemental powders (Figure 3a) was dissolved and formed HfNbTaTiZr alloy (Figure 3b–d). The matrix had a chemical composition close to the equimolar composition in all sintered specimens (see Table 1). Numerous chemical heterogeneities in the “2h”, “4h” and “8h” specimens (highlighted in the “2h” specimen—Figure 3b) could be clearly observed. Their occurrence diminished with an increasing sintering time and in the specimens sintered for 16 h (or more) could only be rarely seen (Figure 3c,d). The heterogeneities were identified as areas with an increased Ta content. However, their number and volume fraction were lower than the fraction of Ta powder in the original powder blend. No areas with significantly higher Nb (or other elements except for Ta) content that could be ascribed to insufficient dissolution of the original powder particles were observed in any of the sintered specimens. According to EBSD analysis (not shown here), neither the sintered nor annealed specimens exhibited any preferred grain orientation (texture).

**Table 1.** Average chemical composition (in at.%) of observed phases indicated in Figure 3e.

Phase	Ti	Zr	Nb	Hf	Ta
Matrix bcc	19.9 ± 0.5	19.0 ± 1.3	21.1 ± 1.6	20.2 ± 0.9	19.8 ± 1.7
precipitate bcc2	22.0 ± 2.1	7.0 ± 1.4	28.3 ± 2.8	11.1 ± 1.2	31.3 ± 3.4
precipitate hcp	7.7 ± 1.5	40.7 ± 1.6	6.5 ± 2.5	38.8 ± 3.0	7.8 ± 3.0

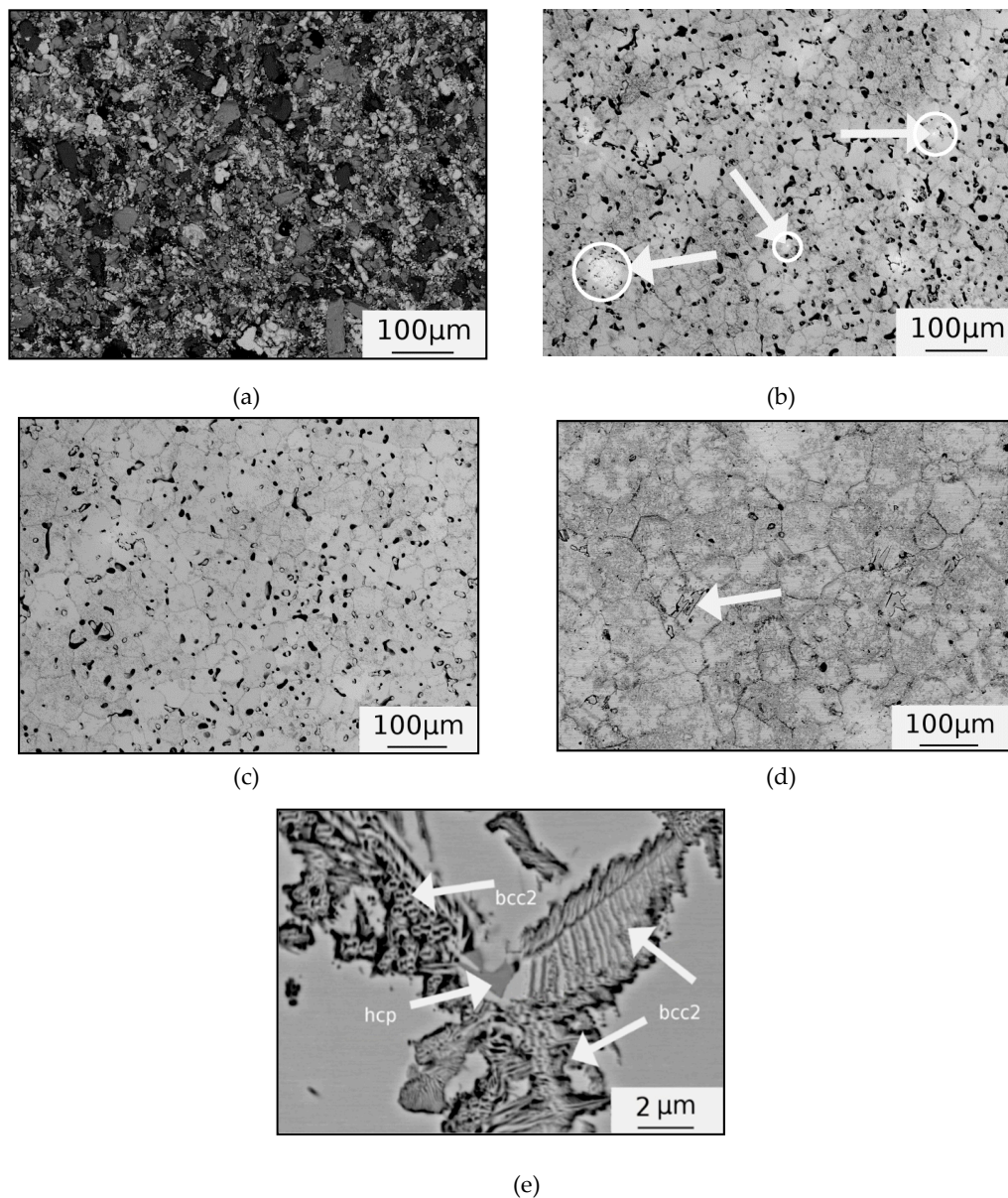


**Figure 3.** Microstructure of specimens shown in scanning electron microscopy (SEM)—back-scattered electron (BSE) mode: (a) pressed powders before sintering; (b) sintered 1400 °C/2h—areas with increased Ta content are marked by arrows; (c) sintered 1400 °C/16h; (d) sintered 1400 °C/64h—coarse hcp phase marked by arrow; (e) sintering 1400 °C/8h.

Numerous precipitates can be seen in the microstructure of the sintered specimens (Figures 3–5). An example of the XRD pattern of sample “64h” is plotted in Figure 6a. The XRD analysis confirmed the presence of two bcc and one hcp phases. Additionally, a very small fraction (<1 wt.%) of (Hf, Zr)O<sub>2</sub> oxides was detected in the “64h” specimen. This could be ascribed either to the local contamination of the specimen or to a higher oxygen content (see Figure 2) which may lead to (Hf, Zr)O<sub>2</sub> formation. The dominating phase, i.e., matrix, denoted here as “bcc”, has the bcc structure with the lattice parameter  $a = 3.399(8) \text{ \AA}$  and its chemical composition is close to the equimolar concentration HfNbTaTiZr (see Table 1). The bcc matrix contains precipitates which have either a bcc or a hcp structure. The precipitates with a bcc structure, denoted “bcc2”, exhibit a lattice parameter  $a = 3.347(3) \text{ \AA}$ , which is lower than that of the bcc matrix. According to EDS analysis, the bcc2 precipitates are enriched in Ta and Nb (see Table 1). The precipitates with hcp structure, denoted “hcp”, are characterized by

lattice parameters  $a = 3.205(3) \text{ \AA}$  and  $c = 5.113(7) \text{ \AA}$  and are rich in Hf and Zr (see Table 1). It was determined by XRD analysis that the fraction of the Zr- and Hf-rich phase (hcp) is lower than that of the Ta- and Nb-rich phase (bcc2) in the sintered specimens (see Table 2), which is consistent with the SEM observations (Figure 3d,e). One type of precipitate is located both in the vicinity of the grain boundaries and in the grain interiors (see Figure 3d,e). The EDS analysis revealed that both of these precipitates are Ta- and Nb-rich phases (i.e., bcc2 phase; see Table 1). Other precipitates of irregular shapes could be observed along the grain boundaries (also depicted with arrows in Figure 3e). These precipitates were typically smaller in size (up to  $1 \mu\text{m}$ ). They were indexed as hcp phase according to TEM-SAED analysis (Figure 5) and were enriched with Zr and Hf (see Table 1). It has to be mentioned that, in some cases (especially for the hcp phase), the precipitates were so fine that the EDS signal could partly originate from the surrounding area. Due to this reason, more measurements were taken throughout all the specimens and the values summarized in Table 1 are the average chemical compositions. Additionally, the significantly coarser (few tens of  $\mu\text{m}$ ) hcp precipitates (Hf- and Zr-rich) were observed along the edge of the specimens (Figure 4) and locally also inside the “64h” specimen (see Figure 3d depicted by a white arrow). These precipitates were of a similar irregular shape to the fine ones. According to TEM-SAED analysis, the hcp precipitates had an orientation relationship with the matrix  $\{110\}_{\text{matrix}}//\{0001\}_{\text{hcp}}$  and  $[001]_{\text{matrix}}//[\bar{2}1\bar{1}0]_{\text{hcp}}$  (Figure 5).

**Table 2.** Weight fractions of phases detected by XRD.

Specimen	bcc	hcp (Zr- and Hf-rich)	bcc2 (Ta- and Nb-rich)
“2 h”	68.5%	5%	26.5%
“4 h”	59.5%	11.3%	29.2%
“8 h”	65.6%	11.6%	22.8%
“16 h”	65.0%	6.8%	28.2%
“32 h”	58.5%	13%	28.5%
“64 h” *	52.2%	5.3%	41.3%
“2 h” + 1200 °C/1 h/WQ	87.5%	12.5%	-
“4 h” + 1200 °C/1 h/WQ	91.8%	8.2%	-
“8 h” + 1200 °C/1 h/WQ	95.3%	4.7%	-
“16 h” + 1200 °C/1 h/WQ	94.4%	5.6%	-
“32 h” + 1200 °C/1 h/WQ	94.6%	5.4%	-
“64 h” + 1200 °C/1 h/WQ	92.1%	7.9%	-

\* This specimen also contained a very small fraction of (Hf, Zr)O<sub>2</sub> oxide.

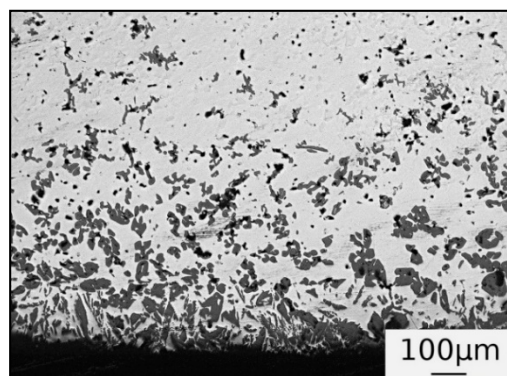


**Figure 4.** Microstructure after sintering at 1400 °C/64h. The specimen surface area at the bottom (LM).

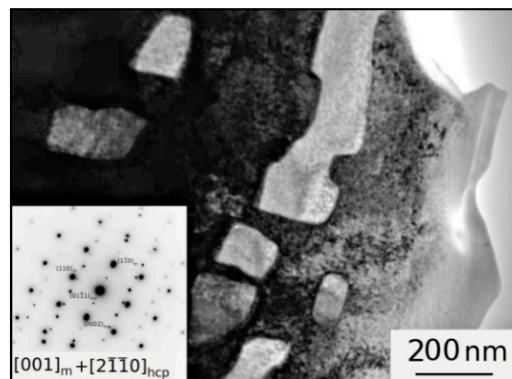


**Figure 5.** Microstructure with hcp phase after sintering at 1400 °C/16h with the diffraction pattern (TEM-SAED).

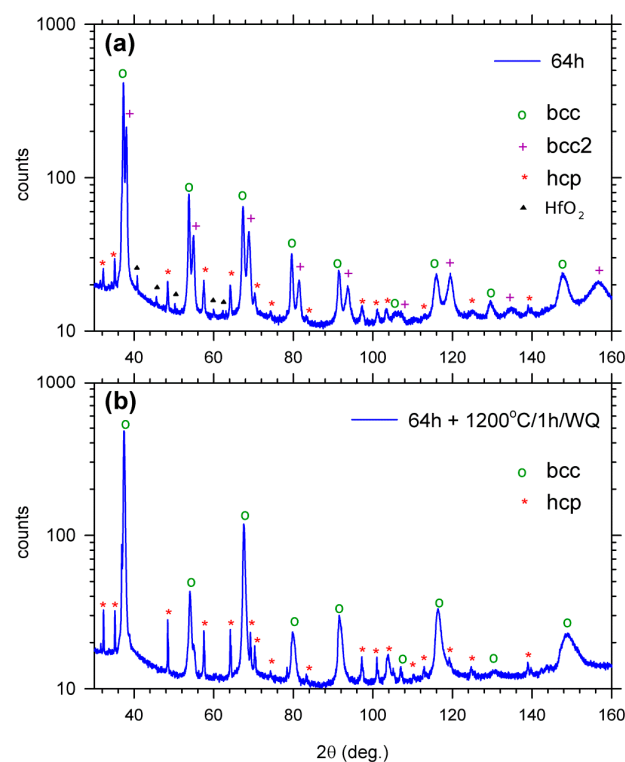


**Figure 6.** X-ray diffraction (XRD) pattern for (a) sample “64h”; (b) sample “64h+1200 °C/1h/WQ”.

An example of the XRD pattern of sample “64h+1200 °C/1h/WQ” is plotted in Figure 6b. In contrast to the as-sintered samples, no bcc2 phase was detected in the samples annealed at 1200 °C for 1 h and water quenched. The XRD analysis of the 1200 °C/1h/WQ samples revealed only the presence of a single bcc phase (matrix) with slightly broadened peaks and a certain fraction of the hcp (Hf, Zr-rich) phase (Table 2). The microstructure of the quenched samples consisted of equiaxed grains with numerous fine precipitates located both along the grain boundaries and inside the grain interiors (see Figure 7). The TEM analysis (see Figure 8) proved that the fine precipitates in the solution-treated specimens were hcp particles with the same orientation relationship  $\{110\}_{\text{matrix}}//\{0001\}_{\text{hcp}}$  and  $[001]_{\text{matrix}}//[2\bar{1}\bar{1}0]_{\text{hcp}}$  as in the as-sintered specimens. Water quenching also resulted in the emergence of cracks within some specimens, which indicated a high internal stress caused by the high cooling rate and limited plasticity at room temperature.

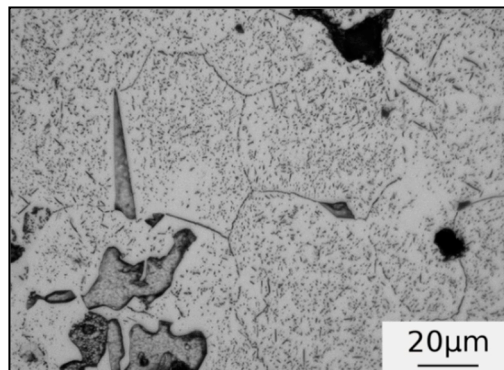


**Figure 7.** Microstructure of the 64h + 1200 °C/1h/WQ sample with a coarse and fine hcp phase (LM).

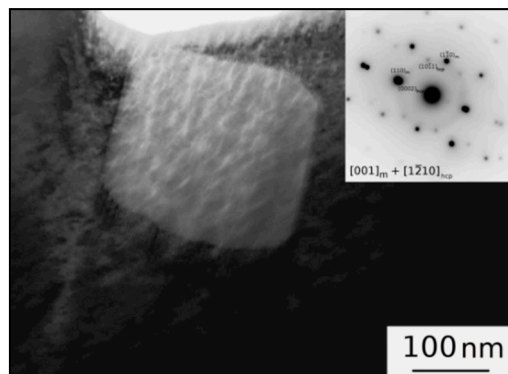


**Figure 8.** Microstructure of the 64h + 1200 °C/1h/WQ sample with a hcp phase (TEM-SAED).

The average grain size is plotted in Figure 9 as a function of the sintering time at 1400 °C. The mean grain size increased with the sintering period from 25 μm after 2 h of sintering to 60 μm after 64 h of sintering. The grain size of each specimen remained unchanged (with respect to the experimental scatter) during 1200 °C/1h annealing.

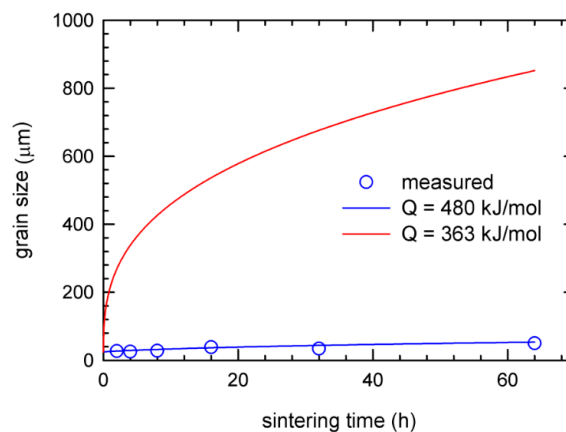


**Figure 9.** Grain size vs. sintering time. Experimental data are plotted by circles; the development of grain size calculated using Equation (1) (see in chapter 4. Discussion) for  $Q = 363$  kJ/mol and  $Q = 480$  kJ/mol is plotted by solid lines.

The DSC curves for the sintered samples heated at the heating rate of 7 °C/min (Figure 10) show a significant endothermic peak starting at approximately 1050 °C with a maximum at around 1300–1350 °C. The endothermic peak can be attributed to the dissolution of the secondary phases (bcc2 and hcp). In order to find the origin of the endothermic peak, DSC measurements were also taken



of the samples annealed at 1200 °C and quenched in water. The DSC curve of the “16h+1200 °C/1h/WQ” sample plotted in Figure 10c exhibits a similar endothermic peak to the sintered alloys (Figure 10a,b). Note that the DSC curve of the sample “64h” contains two separated endothermic peaks. The peak in the range 1250–1450 °C, ascribed to dissolution of the hcp phase, is preceded by an endothermic peak occurring in the temperature range 1050–1250 °C (see Figure 10d).

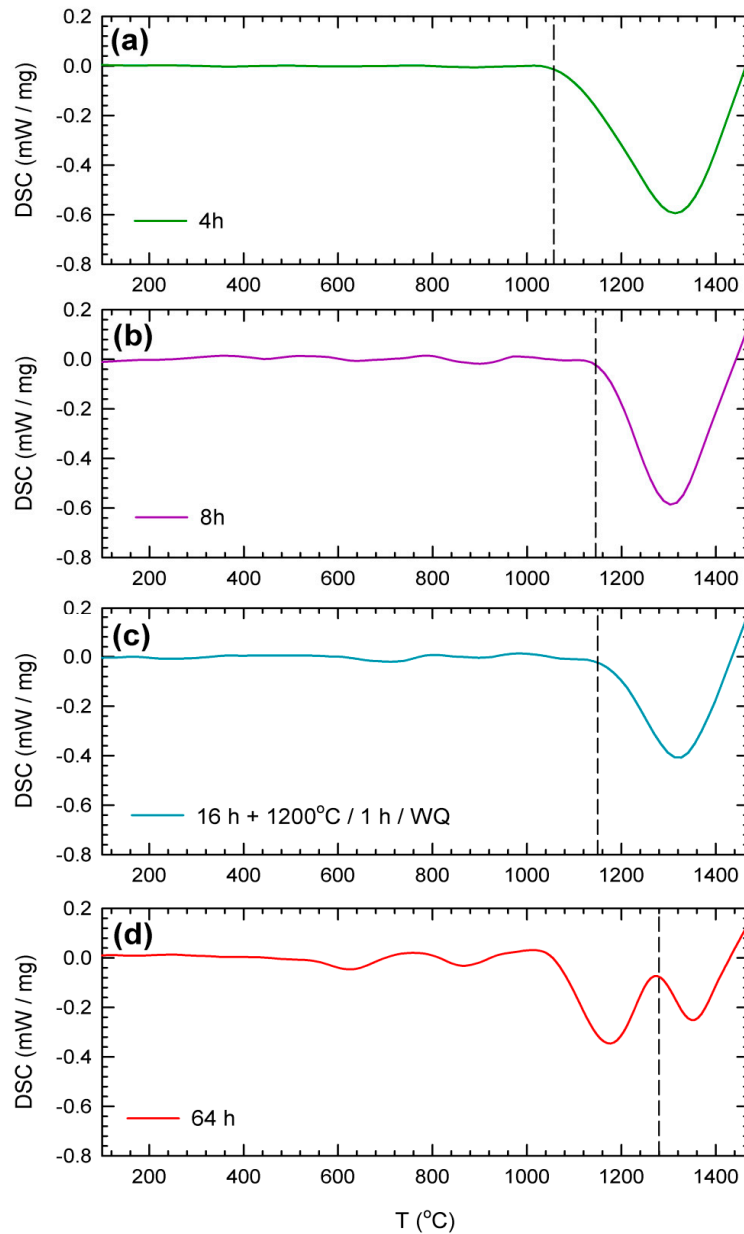


**Figure 10.** DSC curves for the samples heated at the heating rate of 7 °C/min. The vertical dashed line indicates the onset of the endothermic peak ascribed to the dissolution of the hcp phase. (a) 4 h, (b) 8 h, (c) 16 h + 1200 °C/1 h/WQ, (d) 64 h.

### 3.2. Mechanical Properties

The hardness increases with the increasing sintering time period, as can be seen in Figure 11. The hardness values have a relatively large experimental scatter, which is probably caused by the residual porosity, and partly also by chemical inhomogeneities (especially within specimens after shorter sintering periods).

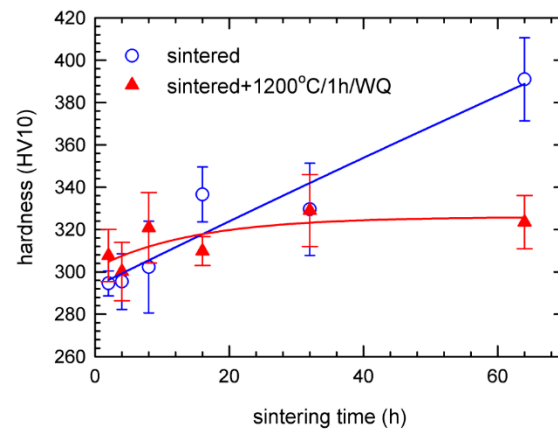


**Figure 11.** The development of hardness with the sintering time for the samples after sintering and the samples subjected to annealing at 1200 °C/water quenched.

The results of the compression tests of the “16h” specimens are summarized in Figure 12. The tests were performed at the strain rate of  $10^{-4} \text{ s}^{-1}$  at elevated temperatures. As can be seen from the figure, the ultimate compressive strength was the highest at 800 °C (approx. 370 MPa) and then decreased at 900 °C, and again at 1000 °C; the further decrease in strength after increasing the temperature above 1000 °C was not significant. A lowest strength of 47 MPa was acquired for the 1200 °C sample.

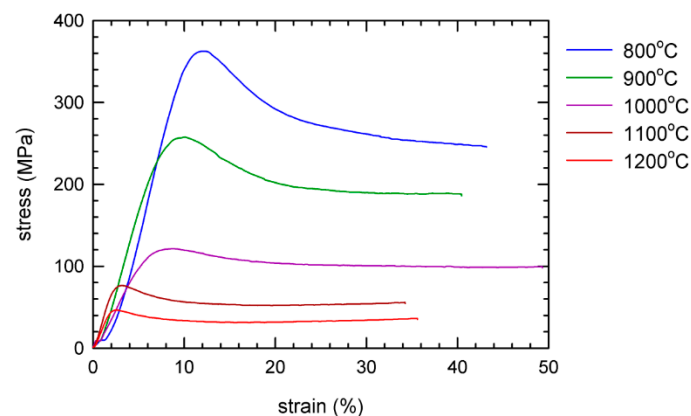


**Figure 12.** Compression stress-strain curves for the “16h” as-sintered specimen at elevated temperatures.

The microstructural observations performed after the compression tests showed that the residual porosity was completely removed in the central region of all of the specimens (see Figure 13a). Some porosity remained at the edge of all of the specimens regardless of the test temperature (the largest area with remaining porosity can be found in the specimen after the 800 °C compression test). It should be pointed out that some flow instabilities could be observed at specimens deformed at 800, 900 and 1000 °C (see Figure 13b). It was less distinct in specimens tested at 1000 °C. No such effects could have been observed after testing at 1100 °C and 1200 °C (Figure 13b). More detailed experiments focusing on the full densification of the current alloy will be performed and published soon in a separate paper. The hardness was measured in the pore-free region of the specimens after the compression tests. All of the specimens showed hardness values of around 450 HV10 within the experimental scatter except for the specimen deformed at 800 °C, which exhibited hardness of  $415 \pm 20$  HV10.

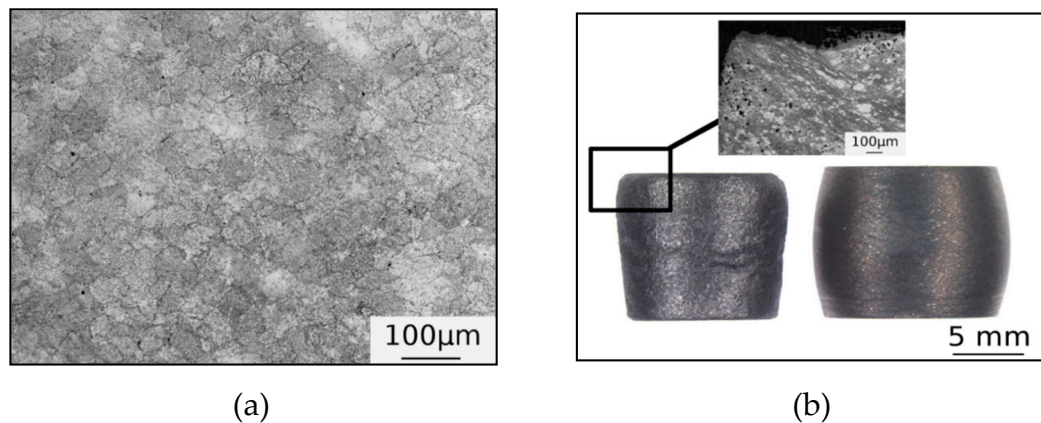


**Figure 13.** Microstructure of specimens after the compression test. (a) Central region (pore free) of the “16h” specimen after the compression test at 900 °C; (b) “16h” specimens after hot compression tests at 800 °C (left) with flow instabilities—see inset and at 1100 °C (right).

#### 4. Discussion

Several changes in microstructure during sintering were probably caused mainly by the diffusion processes. The porosity decreased (Figure 1) due to the reduction in the free surface energy, as was reported by many authors (e.g., [48–50]). The decrease was more significant during the first period of sintering. Also, the increasing oxygen content with the increasing sintering time (Figure 2) can possibly be attributed to spare oxygen in the vacuum (despite the fact that a vacuum better than  $10^{-3}$  Pa was retained during the process) and its subsequent diffusion into the alloy. Some of the used elements (i.e., Ti, Zr, and Hf) are highly reactive with oxygen (especially at high temperatures). However, this was not the only source of oxygen, which is clear from the fact that as-pressed (non-sintered) specimens also contained a relatively high amount of oxygen. Most of the oxygen was introduced to the powders during their synthesis.

The presence of Ta-rich areas shown in Figure 3b in the specimens sintered for short periods (mainly 2, 4 and 8 h) was probably caused by the fact that the original Ta particles were not fully dissolved during such sintering times. Mainly, the coarsest Ta grains or random Ta agglomerates were not fully dissolved (unlike the finer Ta particles). The fact that the diffusivity of Ta in such alloys is smaller than that of the other used elements was reported previously (self-diffusivity of Ta is  $\sim 10$  times lower than that for the Nb and  $\sim 10^{10}$  lower than for the other used elements)[20].

The phase composition of the sintered specimens consisted of the bcc matrix and hcp and bcc2 phases, which was confirmed by SEM, TEM and XRD. Broadening of the XRD peaks of the bcc phase was observed, probably due to variations in the matrix chemical composition. The presence of these phases in the HfNbTaTiZr alloy has been reported in the literature [31,33,38,51,52], but the observed orientation relationship between the matrix and hcp is different from that observed by Chen et al. [51].

The thermal stability of the observed phases in this paper is different from what was reported in the literature. Various authors claimed that the HfNbTaTiZr alloy is a single-phase random solution with a bcc structure only at temperatures above 1000 °C [19,20,38]. Sometimes, slightly higher (1020 °C by Schuh et al. [19]) or slightly lower (985 °C by Senkov et al. [52]) temperatures have been reported. The alloy maintains the random solid solution bcc phase at lower temperatures (i.e., room temperature) as a metastable phase if the cooling rate is fast enough. The bcc phase decomposition into bcc2 or hcp phases is supposed to emerge during annealing at intermediate temperatures [19,20,51,53]. Sintering can be considered as a long-term annealing (after reaching alloy composition due to the diffusion process). Therefore, the herein studied alloy underwent annealing treatment at 1400 °C (sintering), which was far higher than the temperatures necessary to achieve the stable single bcc phase. Despite this fact, high fractions of bcc2 and also hcp phases were present in all studied specimens after sintering (see Table 2). The volume fraction of both bcc2 and hcp phases shows an increasing trend

with an increasing period of sintering at 1400 °C. Schuh et al. [19] performed Calphad simulations which clearly showed that the start of bcc2 precipitation occurs after cooling below 1020 °C (starting to be intensive at temperatures of 900 °C and lower). The same simulation indicated that the hcp phase emerges around 800 °C and its formation is intensive at 700 °C and lower temperatures. Similar results were obtained by Senkov et al. [52]. These calculations were also confirmed by other authors during real experiments (e.g., [20,38,45,51,53]). Therefore, in this work, a single-phase bcc microstructure could be expected as a result of keeping the samples at high temperature (1400 °C) during sintering. A possible reason for the presence of the bcc2 and hcp phases in the studied alloy is the relatively low cooling rate of the sintered samples in a vacuum furnace. The low cooling rate led to a prolonged period during which the specimens were kept at temperatures that could result in the formation of both bcc2 and hcp phases. Wu et al. [53] claimed that the decomposition of bcc into bcc2 and hcp is possible at a low cooling rate of <15 °C/min, while using a higher cooling rate means that a single bcc phase can be retained as a metastable phase at room temperature [34,45]. In the present work, the furnace cooling rate was approximately 12 °C/min within the temperature range 800–600 °C and ~5 °C/min within the temperature range 600–400 °C. It can therefore be assumed that the cooling rate may play some role in the decomposition of the bcc matrix into the bcc2 and hcp phases. High-temperature annealing has been recently performed by Yang et al. [54], who reported the presence of a hcp phase in a HfNbTaTiZr arc melted alloy after 1200 °C/24h annealing. However, in this case, the alloy was also furnace cooled, but no bcc2 phase was reported. In order to prove the hypothesis of the influence of a low cooling rate on bcc2 and hcp phase formation, the specimens were annealed at 1200 °C for 1 h and water quenched (1200 °C/1h/WQ).

The bcc2 phases were not observed in any specimen after water quenching from the annealing temperature of 1200 °C, indicating that the low cooling rate is the reason for bcc2 formation. On the other hand, the hcp phase is present even after fast cooling. The reason for the presence of hcp phase in 1200 °C/1h/WQ specimens is probably the high oxygen content in the studied alloy (approximately 0.7 wt.%; see Figure 2). Oxygen is known to stabilize the  $\alpha$ -phase (hcp) in Zr, Hf and Ti by shifting the  $\alpha$ - $\beta$  (hcp to bcc) transition to higher temperatures [55,56]. No oxides were detected in the solution-treated alloys, which means that in this case the oxygen was fully dissolved in the interstitial sites in the lattice, despite the fact that its content was far higher than in the previously studied arc melted titanium alloys [57–59], where its content was ~0.1 wt.% (the oxygen in arc melted HEAs was measured to be similar). The high oxygen content may be the reason for the unexpected hcp formation, even during a fast cooling rate (water quenching) in the studied alloy. This hypothesis is also supported by the fact that a higher hcp fraction can be observed near the surface of the sintered specimens (see Figure 4). The surface of the specimen (and the surrounding layer) is supposed to have higher oxygen content as it is in direct contact with the furnace atmosphere (vacuum  $\sim 10^{-3}$  Pa). A more intense formation of the hcp phase can therefore be expected close to the surface of the specimen. Therefore, the high oxygen content can cause hcp (Zr- and Hf-rich) phase formation regardless of the cooling rate.

The DSC results showed endothermic peaks that can be assigned to hcp and bcc2 dissolution. According to the Calphad simulations of the equilibrium phase diagram performed in [48], the hcp and bcc2 phases should disappear at 800 and 1040 °C, respectively. These temperatures are significantly lower than the temperature range corresponding to the endothermic peak of the DSC curves. Since XRD characterization revealed that the 16h+1200 °C/1h/WQ sample contained a hcp phase but not a bcc2 phase (see Table 2), the endothermic peak can be attributed to dissolution of the hcp phase. The shift in the dissolution of the hcp phase to a significantly higher temperature range with respect to the calculated equilibrium phase diagram [48] was most probably due to the stabilization of the hcp phase by the dissolved oxygen. From the inspection of Figure 10, one can conclude that the endothermic peak gradually shifts to higher temperatures with an increasing sintering period. This is in accordance with the stabilizing effect of oxygen, since the concentration of oxygen dissolved in the lattice increases with an increasing period of sintering (see Figure 2). Indeed, Figure 14 shows that there is a clear positive correlation (with a slope of  $\sim 830$  °C/wt.% of O) between the temperature of the onset of

the DSC endothermic peak and the oxygen concentration determined in the corresponding sample. This supports the fact that the higher oxygen content plays an important role in the phase stability in the HfNbTaTiZr alloy.

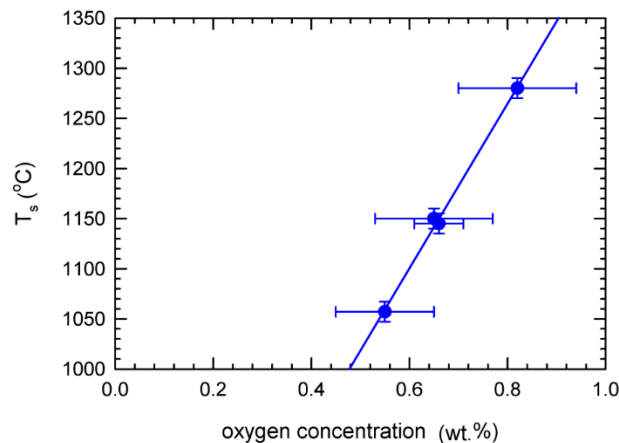


**Figure 14.** The temperature of the onset of the endothermic DSC peak attributed to the dissolution of the hcp phase plotted as a function of the oxygen concentration in the sample.

Two endothermic peaks were clearly observed in the “64h” specimen (Figure 10d). The first in the temperature range 1050–1250 °C was likely caused by the dissolution of the bcc2 phase which, according to the Calphad simulation, takes place at approximately 1040 °C [48]. The effect of dissolution of the bcc2 phase was most pronounced in the 64h sample since it contains the highest volume fraction of the bcc 2 phase among the samples studied (see Table 2). The second peak was assigned to hcp dissolution.

The arc-melted specimens of the HfNbTaTiZr alloy usually exhibit a grain size of a few hundreds of micrometers [16,20]. Sintering can be considered as a high temperature annealing and therefore the observed grain coarsening could be expected. However, the data obtained in our work are inconsistent with data observed by Senkov et al. [20], who reported the following equation (Equation (1)). When using the grain size growth exponent  $n = 3$ , the equation for grain coarsening can be expressed as follows:

$$D^3 - D_0^3 = K_0 e^{-\left(\frac{Q}{RT}\right)} \cdot t. \quad (1)$$

$D$ —grain size ( $\mu\text{m}$ )

$D_0$ —initial grain size ( $\mu\text{m}$ )

$K_0$ —constant =  $5.79 \times 10^{14} (\mu\text{m}^3/\text{s})$

$Q$ —activation energy (J/mol)

$R$ —gas constant (J/K·mol)

$T$ —temperature (K)

$t$ —time (s)

Senkov et al. [20] reported that the activation energy for the HfNbTaTiZr alloy is 363 kJ/mol. Considering the annealing temperature (1400 °C) and initial grain size of  $\sim 25 \mu\text{m}$ , one obtains the development of grain size plotted in Figure 9 by a solid line. Grain sizes predicted by Equation (1) are at least one order of magnitude higher than those observed in the sintered samples. This indicates that the grain coarsening in the sintered samples was suppressed. This phenomenon can be attributed to several processes: (i) the grain boundaries can be pinned by the precipitates or other particles. However, this factor has probably only a minor effect since all the secondary phases are supposed to be dissolved during sintering at 1400 °C; (ii) grain coarsening can also be significantly hindered by the free surfaces (pores), which are present in the current alloy, as proposed by Liu et al. [60] and by Zilnyk et al. [61]; (iii) the oxygen dissolved in the solid solution could also prevent the grain coarsening.

Gil et al. [62] reported that an increasing oxygen content caused a significant increase in the activation energy of grain growth in pure titanium.

According to the results obtained for the sintered samples, the grain growth should be related to a significantly higher activation energy value—the activation energy of  $Q \approx 480$  kJ/mol was estimated. However, more detailed analysis (annealing at various temperatures) is needed to confirm this value and to determine the activation energy more precisely. The value reported here is the apparent activation energy based on the model described by Equation (1) and reported in [20]. Also, other conditions (e.g., previous cold deformation) may influence the resulting grain size as reported in [23]. The grain size after solution treatment (1200 °C/1h/WQ) remained similar to the grain size of sintered specimens (with respect to experimental scatter). Obviously, this alloy (prepared via powder metallurgy—CIP) is more resistant to grain coarsening during sintering (and annealing) than the same alloy prepared via arc melting. Other authors observed significant grain coarsening during the annealing treatment of the arc melted HfNbTaTiZr alloy [16,22].

The increase in hardness with an increasing sintering period is mainly caused by interstitial strengthening, caused by the increasing concentration of oxygen dissolved in the lattice. Also, decreasing residual porosity may have a similar effect. From the study of  $\beta$ -Ti alloys, it is known that oxygen can significantly increase the tensile strength and change the deformation mechanisms [63]. Also, the hardness of hot deformed (without residual porosity) specimens showed significantly higher hardness values (i.e., 450 HV10) than the hardness of arc melted HfNbTaTiZr specimens, which is reported to be 300–350 HV10 [19,44,45,64]. This difference can be ascribed to the strengthening effect of oxygen (interstitial strengthening).

The value of the compression strength at 800 °C was lower than the value acquired by Senkov et al. [16] for the identical strain rate for the arc melted alloy (~450 MPa). This decrease could partly be affected by the residual porosity, which can reduce the compression strength significantly. Also, in this case, the fine grain size could have a negative effect on the compression strength at elevated temperatures (at a given low strain rate) due to grain boundary sliding. On the other hand, high oxygen content is supposed to cause significant strengthening, as mentioned above (no information about the oxygen content in the alloy was given by Senkov et al. [16,64], but it can be assumed that the oxygen content should be similar to arc melted alloys ~0.1 wt.%).

## 5. Conclusions

The HfNbTaTiZr alloy was synthesized from elemental powders via the powder metallurgy process consisting of mixing, cold isostatic pressing and sintering. The relationship between the microstructure and mechanical properties with the sintering time period was studied. On the basis of the obtained results, the following can be concluded:

(i) Certain residual porosity is present even after the 1400 °C/64h sintering. The chemical homogeneity is satisfactory for the sintering time periods of 16h (and longer), which can therefore be considered as a suitable time period for sintering of elemental powders. The porosity was fully removed in the central regions of specimens during hot deformation.

(ii) The decomposition of the bcc matrix into the bcc2 and hcp phases took place during the furnace cooling after sintering. A fast cooling rate after 1200 °C/1h annealing suppressed the formation of the bcc2 phase, but the hcp phase was still present in the microstructure, probably due to its stabilization via high oxygen content in the alloy.

(iii) The presented powder metallurgy process led to the production of an alloy which is significantly more resistant to grain coarsening when compared to the same alloy prepared via arc melting. Yet this alloy has relatively high oxygen content which can lead to some difficulties during further processing.

**Author Contributions:** Conceptualization, J.M. and J.Z.; methodology, J.M. and J.Č.; validation, J.M., F.L., J.Č. and R.K.; investigation J.M., F.L., J.Č. and L.K.; resources, J.M.; writing—original draft preparation, J.M.; writing—review and editing, J.Z., J.Č. and L.K.; visualization, J.M. and J.Č.; supervision, J.M.; project administration, J.M.; funding acquisition, J.Č.

**Funding:** Support by the Czech Science Foundation (project 17-17016S) is highly acknowledged.

**Acknowledgments:** Special thanks are dedicated to Dr. Jiří Dvořák from VŠB-TU Ostrava for his help with compression tests.

**Conflicts of Interest:** The authors declare no conflict of interest.

## References

1. Miracle, D.B.; Senkov, O.N. Acta Materialia A critical review of high entropy alloys and related concepts. *Acta Mater.* **2017**, *122*, 448–511. [[CrossRef](#)]
2. Yeh, B.J.; Chen, S.K.; Lin, S.J.; Gan, J.Y.; Chin, T.S.; Shun, T.T.; Tsau, C.H.; Chang, S.Y. Nanostructured High-Entropy Alloys with Multiple Principal Elements: Novel Alloy Design Concepts and Outcomes. *Adv. Eng. Mater.* **2004**, *6*, 299–303. [[CrossRef](#)]
3. Cantor, B.; Chang, I.T.H.; Knight, P.; Vincent, A.J.N. Microstructural development in equiatomic multicomponent alloys. *Mater. Sci. Eng. A* **2004**, *375–377*, 213–218. [[CrossRef](#)]
4. Kocich, R.; Kunčická, L.; Davis, C.F.; Lowe, T.C.; Szurman, I.; Macháčková, A. Deformation behavior of multilayered Al–Cu clad composite during cold-swaging. *Mater. Des.* **2016**, *90*, 379–388. [[CrossRef](#)]
5. Kocich, R.; Kunčická, L.; Macháčková, A.; Šofer, M. Improvement of mechanical and electrical properties of rotary swaged Al–Cu clad composites. *Mater. Des.* **2017**, *123*, 137–146. [[CrossRef](#)]
6. Zhang, Y.; Zuo, T.T.; Tang, Z.; Gao, M.C.; Dahmen, K.A.; Liaw, P.K.; Lu, Z.P. Microstructures and properties of high-entropy alloys. *Prog. Mater. Sci.* **2014**, *61*, 1–93. [[CrossRef](#)]
7. Senkov, O.N.; Miracle, D.B. A new thermodynamic parameter to predict formation of solid solution or intermetallic phases in high entropy alloys. *J. Alloys Compd.* **2016**, *658*, 603–607. [[CrossRef](#)]
8. Ye, Y.F.; Wang, Q.; Lu, J.; Liu, C.T.; Yang, Y. High-entropy alloy: Challenges and prospects. *Mater. Today* **2016**, *19*, 349–362. [[CrossRef](#)]
9. Cao, Y.; Liu, Y.; Liu, B.; Zhang, W. Precipitation behavior during hot deformation of powder metallurgy Ti–Nb–Ta–Zr–Al high entropy alloys. *Intermetallics* **2018**, *100*, 95–103. [[CrossRef](#)]
10. Yang, X.; Zhang, Y. Prediction of high-entropy stabilized solid-solution in multi-component alloys. *Mater. Chem. Phys.* **2012**, *132*, 233–238. [[CrossRef](#)]
11. Vrtnik, S.; Lužnik, J.; Koželj, P.; Jelen, A.; Luzar, J.; Krnel, M.; Jagličič, Z.; Meden, A.; Fuerbacher, M.; Dolinšek, J. Magnetic phase diagram and magnetoresistance of Gd–Tb–Dy–Ho–Lu hexagonal high-entropy alloy. *Intermetallics* **2019**, *105*, 163–172. [[CrossRef](#)]
12. Zhao, Y.J.; Qiao, J.W.; Ma, S.G.; Gao, M.C.; Yang, H.J.; Chen, M.W.; Zhang, Y. A hexagonal close-packed high-entropy alloy: The effect of entropy. *Mater. Des.* **2016**, *96*, 10–15. [[CrossRef](#)]
13. Yusenko, K.V.; Riva, S.; Carvalho, P.A.; Yusenko, M.V.; Arnaboldi, S.; Suknikh, A.S.; Hanfland, M.; Gromilov, S.A. First hexagonal close packed high-entropy alloy with outstanding stability under extreme conditions and electrocatalytic activity for methanol oxidation. *Scr. Mater.* **2017**, *138*, 22–27. [[CrossRef](#)]
14. Fuerbacher, M.; Heidelmann, M.; Carsten, T. Hexagonal High-Entropy Alloys. *Mater. Res. Lett.* **2015**, *3*, 1–6. [[CrossRef](#)]
15. Chang, C.; Titus, M.S.; Yeh, J. Oxidation Behavior between 700 and 1300 C of Refractory TiZrNbHfTa High-Entropy Alloys Containing Aluminum. *Adv. Eng. Mater.* **2018**, *20*, 1–8. [[CrossRef](#)]
16. Senkov, O.N.; Scott, J.M.; Senkova, S.V.; Maisenkothen, F.; Miracle, D.B.; Woodward, C.F. Microstructure and elevated temperature properties of a refractory TaNbHfZrTi alloy. *J. Mater. Sci.* **2012**, *47*, 4062–4074. [[CrossRef](#)]
17. Kunčická, L.; Kocich, R.; Hervoches, C.; Macháčková, A. Study of structure and residual stresses in cold rotary swaged tungsten heavy alloy. *Mater. Sci. Eng. A* **2017**, *704*, 25–31. [[CrossRef](#)]
18. Dirras, G.; Lilenstein, L.; Djemia, P.; Laurent-Brocq, M.; Tingaud, D.; Couzinie, J.P.; Perriere, L.; Chauveau, T.; Guillot, I. Elastic and plastic properties of as-cast equimolar TiHfZrTaNb high-entropy alloy. *Mater. Sci. Eng. A* **2016**, *654*, 30–38. [[CrossRef](#)]
19. Schuh, B.; Volker, B.; Todt, J.; Schnell, N.; Perriere, L.; Li, J.; Couzinie, J.P.; Hohenwarter, A. Thermodynamic instability of a nanocrystalline, single-phase TiZrNbHfTa alloy and its impact on the mechanical properties. *Acta Mater.* **2018**, *142*, 201–212. [[CrossRef](#)]

20. Senkov, O.N.; Pilchak, A.L.; Semiatin, S.L. Effect of Cold Deformation and Annealing on the Microstructure and Tensile Properties of a HfNbTaTiZr Refractory High Entropy Alloy. *Metall. Mater. Trans. A* **2018**, *49*, 2876–2892. [[CrossRef](#)]
21. Zyka, J.; Málek, J.; Pala, Z.; Andršová, I.; Vesely, J. Structure and mechanical properties of TaNbHfZrTi high entropy alloy. In Proceedings of the METAL 2015—24th International Conference on Metallurgy and Materials, Brno, Czech Republic, 3–5 June 2015.
22. Juan, C.C.; Tsai, M.H.; Tsai, C.W.; Hsu, W.L.; Lin, C.M.; Chen, S.K.; Lin, S.J.; Yeh, J.W. Simultaneously increasing the strength and ductility of a refractory high-entropy alloy via grain refining. *Mater. Lett.* **2016**, *184*, 200–203. [[CrossRef](#)]
23. Chen, S.; Tseng, K.K.; Tong, Y.; Li, W.; Tsai, C.W.; Yeh, J.W.; Liaw, P.K. Grain growth and Hall-Petch relationship in a refractory HfNbTaZrTi high-entropy alloy. *J. Alloys Compd.* **2019**, *795*, 19–26. [[CrossRef](#)]
24. Eisenbarth, E.; Velten, D.; Müller, M.; Thull, R.; Breme, J. Biocompatibility of  $\beta$ -stabilizing elements of titanium alloys. *Biomaterials* **2004**, *25*, 5705–5713. [[CrossRef](#)] [[PubMed](#)]
25. Grandin, H.M.; Berner, S.; Dard, M. A review of Titanium Zirconium (TiZr) alloys for use in endosseous dental implants. *Materials* **2012**, *5*, 1348–1360. [[CrossRef](#)]
26. Biesiekierski, A.; Wang, J.; Abdel-Hady Gepreel, M.; Wen, C. A new look at biomedical Ti-based shape memory alloys. *Acta Biomater.* **2012**, *8*, 1661–1669. [[CrossRef](#)]
27. Kunčická, L.; Kocich, R.; Lowe, T.C. Advances in metals and alloys for joint replacement. *Prog. Mater. Sci.* **2017**, *88*, 232–280. [[CrossRef](#)]
28. Kocich, R.; Kursá, M.; Szurman, I.; Dlouhý, A. The influence of imposed strain on the development of microstructure and transformation characteristics of Ni–Ti shape memory alloys. *J. Alloys Compd.* **2011**, *509*, 2716–2722. [[CrossRef](#)]
29. Couzinie, J.P.; Dirras, G.; Perriere, L.; Chauveau, T.; Leroy, E.; Champion, Y.; Guillot, I. Microstructure of a near-equimolar refractory high-entropy alloy. *Mater. Lett.* **2014**, *126*, 285–287. [[CrossRef](#)]
30. Poletti, M.G.; Fiore, G.; Szost, B.A.; Battezzati, L. Search for high entropy alloys in the X-NbTaTiZr systems (X = Al, Cr, V, Sn). *J. Alloys Compd.* **2015**, *620*, 283–288. [[CrossRef](#)]
31. Yao, J.Q.; Liu, X.W.; Gao, N.; Jiang, Q.H.; Li, N.; Liu, G.; Zhang, W.B.; Fan, Z.T. Phase stability of a ductile single-phase BCC Hf<sub>0.5</sub>Nb<sub>0.5</sub>Ta<sub>0.5</sub>Ti<sub>1.5</sub>Zr refractory high-entropy alloy. *Intermetallics* **2018**, *98*, 79–88. [[CrossRef](#)]
32. Guo, N.N.; Wang, L.; Luo, L.S.; Li, X.Z.; Su, Y.Q.; Guo, J.J.; Fu, H.Z. Microstructure and mechanical properties of refractory MoNbHfZrTi high-entropy alloy. *Mater. Des.* **2015**, *81*, 87–94. [[CrossRef](#)]
33. Todai, M.; Nagase, T.; Hori, T.; Matsugaki, A.; Sekita, A.; Nakano, T. Novel TiNbTaZrMo high-entropy alloys for metallic biomaterials. *Scr. Mater.* **2017**, *129*, 65–68. [[CrossRef](#)]
34. Juan, C.C.; Tseng, K.K.; Hsu, W.L.; Tsai, M.H.; Tsai, C.W.; Lin, C.M.; Chen, S.K.; Lin, S.J.; Yeh, J.W. Solution strengthening of ductile refractory HfMo x NbTaTiZr high-entropy alloys. *Mater. Lett.* **2016**, *175*, 284–287. [[CrossRef](#)]
35. Juan, C.C.; Tsai, M.H.; Tsai, C.W.; Lin, C.M.; Wang, W.R.; Yang, C.C.; Chen, S.K.; Lin, S.J.; Yeh, J.W. Enhanced mechanical properties of HfMoTaTiZr and HfMoNbTaTiZr refractory high-entropy alloys. *Intermetallics* **2015**, *62*, 76–83. [[CrossRef](#)]
36. Maiti, S.; Steurer, W. Structural-disorder and its effect on mechanical properties in single-phase TaNbHfZr high-entropy alloy. *Acta Mater.* **2016**, *106*, 87–97. [[CrossRef](#)]
37. Dirras, G.; Couque, H.; Liliensten, L.; Heczal, A.; Tingaud, D.; Couzinie, J.P.; Perriere, L.; Gubicza, J.; Guillot, I. Mechanical behavior and microstructure of Ti<sub>20</sub>Hf<sub>20</sub>Zr<sub>20</sub>Ta<sub>20</sub>Nb<sub>20</sub> high-entropy alloy loaded under quasi-static and dynamic compression conditions. *Mater. Charact.* **2016**, *111*, 106–113. [[CrossRef](#)]
38. Senkov, O.N.; Semiatin, S.L. Microstructure and properties of a refractory high-entropy alloy after cold working. *J. Alloys Compd.* **2015**, *649*, 1110–1123. [[CrossRef](#)]
39. Dirras, G.; Gubicza, J.; Heczal, A.; Liliensten, L.; Couzinie, J.P.; Perriere, L.; Guillot, I.; Hocini, A. Microstructural investigation of plastically deformed Ti<sub>20</sub>Zr<sub>20</sub>Hf<sub>20</sub>Nb<sub>20</sub>Ta<sub>20</sub> high entropy alloy by X-ray diffraction and transmission electron microscopy. *Mater. Charact.* **2015**, *108*, 1–7. [[CrossRef](#)]
40. Wu, Y.D.; Cai, Y.H.; Chen, X.H.; Wang, T.; Si, J.J.; Wang, L.; Wang, Y.D.; Hui, X.D. Phase composition and solid solution strengthening effect in TiZrNbMoV high-entropy alloys. *Mater. Des.* **2015**, *83*, 651–660. [[CrossRef](#)]



41. Kunčická, L.; Lowe, T.C.; Davis, C.F.; Kocich, R.; Pohludka, M. Synthesis of an Al/Al<sub>2</sub>O<sub>3</sub> composite by severe plastic deformation. *Mater. Sci. Eng. A* **2015**, *646*, 234–241. [[CrossRef](#)]
42. Kocich, R.; Szurman, I.; Kurša, M.; Fiala, J. Investigation of influence of preparation and heat treatment on deformation behaviour of the alloy NiTi after ECAE. *Mater. Sci. Eng. A* **2009**, *512*, 100–104. [[CrossRef](#)]
43. Kang, B.; Lee, J.; Jin, H.; Hyung, S. Ultra-high strength WNbMoTaV high-entropy alloys with fine grain structure fabricated by powder metallurgical process. *Mater. Sci. Eng. A* **2018**, *712*, 616–624. [[CrossRef](#)]
44. Zýka, J.; Málek, J.; Veselý, J.; Lukáč, F.; Čížek, J.; Kuriplach, J.; Melikhova, O. Microstructure and Room Temperature Properties of Different 3 and 4 Element Medium Entropy Alloys from HfNbTaTiZr System. *Entropy* **2019**, *21*, 114. [[CrossRef](#)]
45. Čížek, J.; Haušild, P.; Cieslar, M.; Melikhova, O.; Vlasák, T.; Janeček, M.; Král, R.; Harcuba, P.; Lukáč, F.; Zýka, J.; et al. Strength enhancement of high entropy alloy HfNbTaTiZr by severe plastic deformation. *J. Alloys Compd.* **2018**, *768*, 924–937. [[CrossRef](#)]
46. Lukáč, F.; Dudr, M.; Čížek, J.; Harcuba, P.; Vlasák, T.; Janeček, M. Defects in High Entropy Alloy HfNbTaTiZr Prepared by High Pressure Torsion. *Acta Phys. Pol. A* **2018**, *134*, 891–894. [[CrossRef](#)]
47. Lukac, F.; Dudr, M.; Mušálek, R.; Klečka, J.; Cinert, J.; Čížek, J.; Chráska, T.; Čížek, J.; Melikhova, O.; Kuriplach, J.; et al. Spark plasma sintering of gas atomized high-entropy alloy HfNbTaTiZr. *J. Mater. Res.* **2018**, *33*, 3247–3257. [[CrossRef](#)]
48. Biliński, B. The changes in surface free energy and surface heterogeneity of controlled-porosity glasses. *Colloids Surf. A Physicochem. Eng. Asp.* **1994**, *84*, 265–272. [[CrossRef](#)]
49. Graham, D. The Characterization of Physical Adsorption Systems. I. The Equilibrium Function and Standard Free Energy of Adsorption. *J. Phys. Chem.* **1953**, *57*, 665–669. [[CrossRef](#)]
50. Yates, D.J.C. A Note on some Proposed Equations of State for the Expansion of Rigid Porous Solids on the Adsorption of Gases and Vapours. *Proc. Phys. Soc. Sect. B* **1952**, *65*, 80–81. [[CrossRef](#)]
51. Chen, S.Y.; Tong, Y.; Tseng, K.K.; Yeh, J.W.; Poplawsky, J.D.; Wen, J.G.; Gao, M.C.; Kim, G.; Chen, W.; Ren, Y.; et al. Phase transformations of HfNbTaTiZr high-entropy alloy at intermediate temperatures. *Scr. Mater.* **2019**, *158*, 50–56. [[CrossRef](#)]
52. Senkov, O.N.; Senkova, S.V.; Woodward, C. Effect of aluminum on the microstructure and properties of two refractory high-entropy alloys. *Acta Mater.* **2014**, *68*, 214–228. [[CrossRef](#)]
53. Wu, W.; Ni, S.; Liu, Y.; Song, M. Effects of cold rolling and subsequent annealing on the microstructure of a HfNbTaTiZr high-entropy alloy. *J. Mater. Res.* **2016**, *31*, 3815–3823. [[CrossRef](#)]
54. Yang, C.; Aoyagi, K.; Bian, H.; Chiba, A. Microstructure evolution and mechanical property of a precipitation-strengthened refractory high-entropy alloy HfNbTaTiZr. *Mater. Lett.* **2019**, *254*, 46–49. [[CrossRef](#)]
55. Krejčí, J.; Vrtílková, V.; Kabátová, J.; Příbyl, T.; Gajdoš, P.; Rada, D.; Šustr, J. High-Temperature Oxidation of a Sponge-Based E110 Cladding Tube Material: Weight Gain and Reaction Layer Kinetics. *Nucl. Technol.* **2018**, *201*, 52–65. [[CrossRef](#)]
56. Okamoto, H. *Phase Diagrams for Binary Alloys—Desk Handbook*; ASM International: Cleveland, OH, USA, 2000.
57. Málek, J.; Hnilica, F.; Veselý, J.; Smola, B.; Bartáková, S.; Vaněk, J. Microstructure and mechanical properties of Ti-35Nb-6Ta alloy after thermomechanical treatment. *Mater. Charact.* **2012**, *66*, 75–82. [[CrossRef](#)]
58. Málek, J.; Veselý, J.; Smola, B.; Kolařík, K. The effect of boron addition on microstructure and mechanical properties of biomedical Ti35Nb6Ta alloy. *Mater. Charact.* **2014**, *96*, 166–176. [[CrossRef](#)]
59. Bartáková, S.; Málek, J.; Prachár, P. The Effect of Oxygen Addition on Microstructure and Mechanical Properties of Various Beta-Titanium Alloys. *JOM* **2019**. [[CrossRef](#)]
60. Liu, Y.; Patterson, B.R. Grain growth inhibition by porosity. *Acta Metall. Mater.* **1993**, *41*, 2651–2656. [[CrossRef](#)]
61. Zilnyk, K.D.; Leite, G.S.; Sandim, H.R.Z.; Rios, P.R. Grain growth inhibition by connected porosity in sintered niobium. *Acta Mater.* **2013**, *61*, 5821–5828. [[CrossRef](#)]
62. Gil, F.J.; Aparicio, C.; Planell, J.A. Effect of Oxygen Content on Grain Growth Kinetics of Titanium. *J. Mater. Synth. Process.* **2003**, *10*, 10–13.

63. Lei, Z.; Liu, X.; Wu, Y.; Wang, H.; Jiang, S.; Wang, S.; Hui, X.; Wu, Y.; Gault, B.; Kontis, P.; et al. Enhanced strength and ductility in a high-entropy alloy via ordered oxygen complexes. *Nature* **2018**, *563*, 546–550. [[CrossRef](#)] [[PubMed](#)]
64. Senkov, O.N.; Scott, J.M.; Senkova, S.V.; Miracle, D.B.; Woodward, C.F. Microstructure and room temperature properties of a high-entropy TaNbHfZrTi alloy. *J. Alloys Compd.* **2011**, *509*, 6043–6048. [[CrossRef](#)]



© 2019 by the authors. Licensee MDPI, Basel, Switzerland. This article is an open access article distributed under the terms and conditions of the Creative Commons Attribution (CC BY) license (<http://creativecommons.org/licenses/by/4.0/>).